Electronic Supplementary Material (ESI) for Energy & Environmental Science.

Supplementary Information

Visualization of regulated nucleation and growth of lithium sulfides for high energy lithium sulfur batteries

Zheng-Long Xu,[a]‡ Sung Joo Kim,[a]‡ Donghee Chang,[a]‡ Kyu-Young Park,[a] Kyun Seong Dae,[b] Khoi Phuong Dao,[b] Jong Min Yuk,[b] Kisuk Kang[a]*

[a] Department of Materials Science and Engineering, Research Institute of Advanced Materials (RIAM), Seoul National University, 1 Gwanak-ro, Gwanak-gu, Seoul 151-742, Republic of Korea. E-mail: matlgen1@snu.ac.kr

[b] Department of Materials Science and Engineering, Korea Advanced Institute of Science and Technology (KAIST), 291 Daejeon 34141, Republic of Korea.

‡ These authors contributed equally to this work.

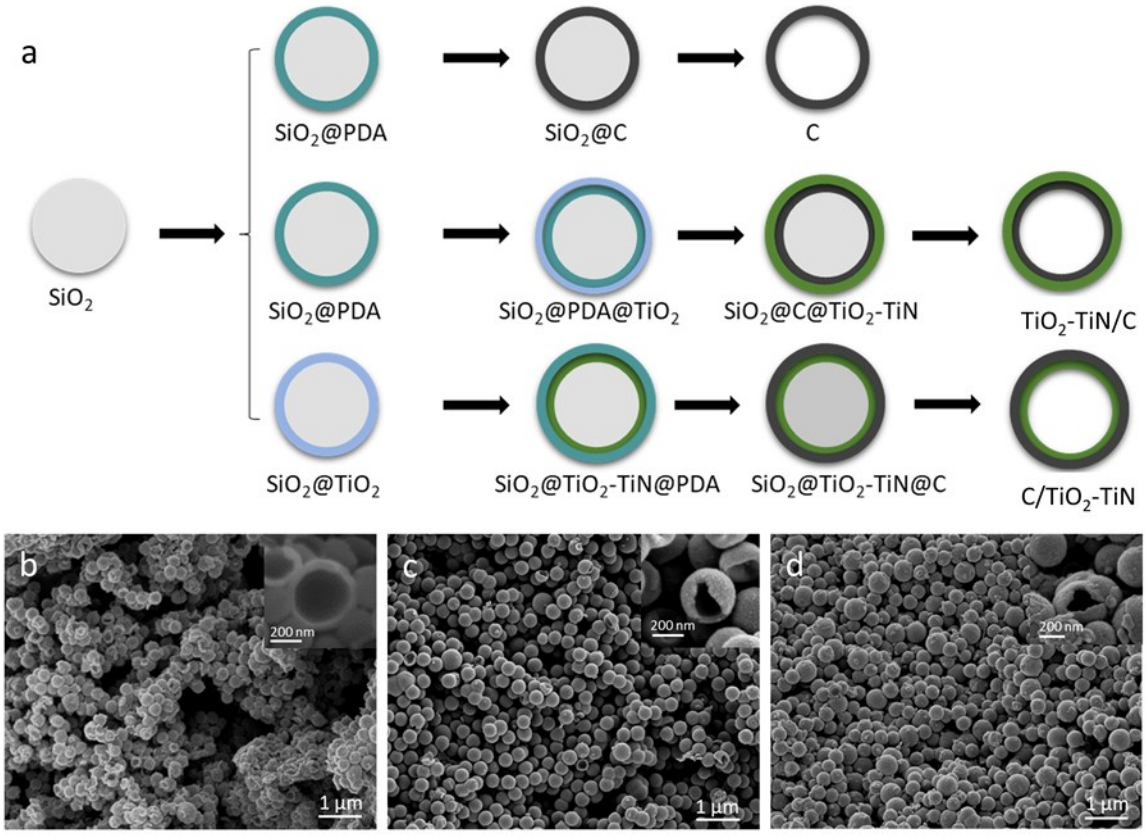

Fig. S1 Preparation and characterization of hollow spheres. (a) Schematic illustration of the procedures to prepare C, TiO_2-TiN/C and C/TiO_2-TiN hollow spheres, SEM images of (b) hollow C, (c) hollow TiO_2-TiN/C and (d) hollow C/TiO_2-TiN. PDA in (a) refers to polydopamine.

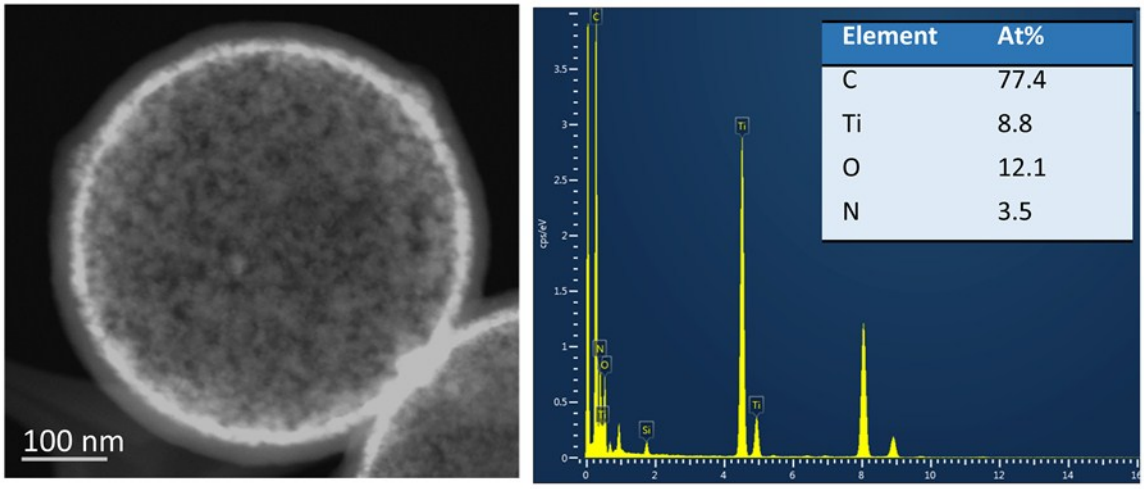

Fig. S2 STEM image and elemental concentration for C/TiO_2-TiN hollow sphere. The molar ratio of TiO_2: TiN is calculated to be approximate 4: 3 based on the element proportions of Ti, N and O.

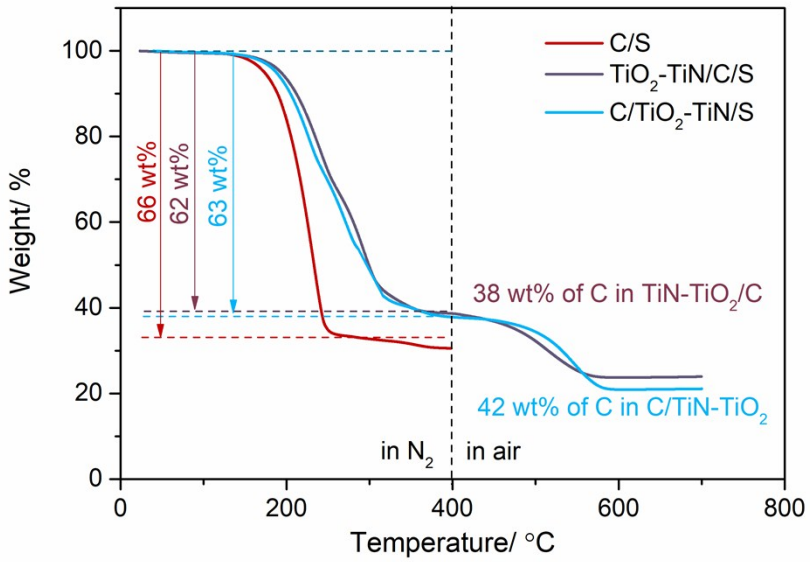

Fig. S3 Chemical compositions of C/S, TiO_2-TiN/C/S and C/TiO_2-TiN/S evaluated by TGA. The samples were heated to 400 °C in N_2 atmosphere, allowing the sulfur contents to be determined as 66 wt%, 62 wt% and 63 wt% for C/S, TiO_2-TiN/C/S and C/TiO_2-TiN/S, respectively. Following, the samples were heated in air to burn carbon materials, thus allowing the evaluation of the carbon content in TiO_2-TiN/C and C/TiO_2-TiN composites.

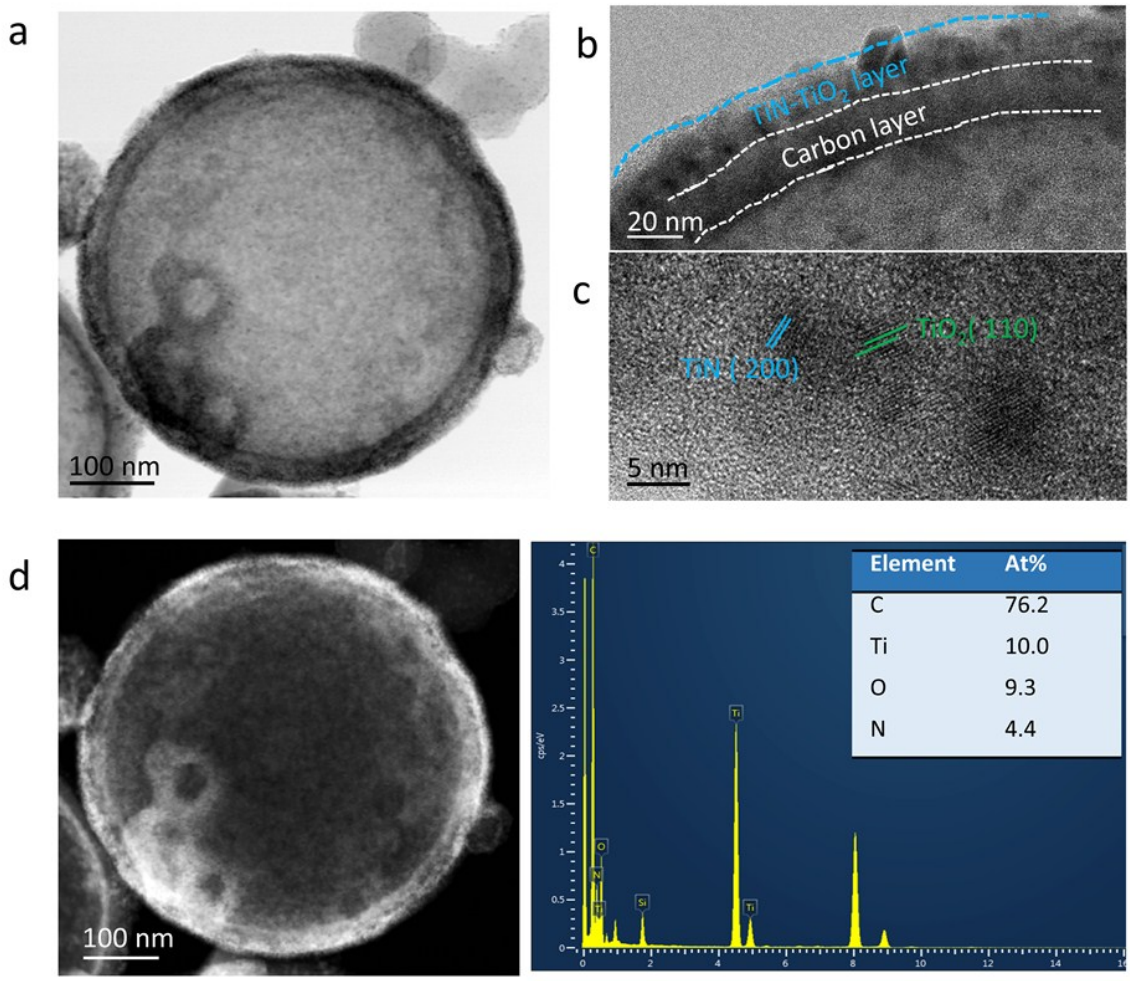

Fig. S4 Morphological and chemical compositions of TiO_2-TiN/C hollow spheres. (a) TEM image of a hollow TiO_2-TiN/C, (b) and (c) HRTEM images showing the TiO_2-TN (outer) and C (inner) walls and crystal structures of TiN and TiO_2, (d) STEM image and elemental concentration for TiO_2-TiN/C hollow spheres. The molar ratio of TiO_2: TiN is calculated to be approximate 4: 3 based on the element proportions of Ti, N and O.

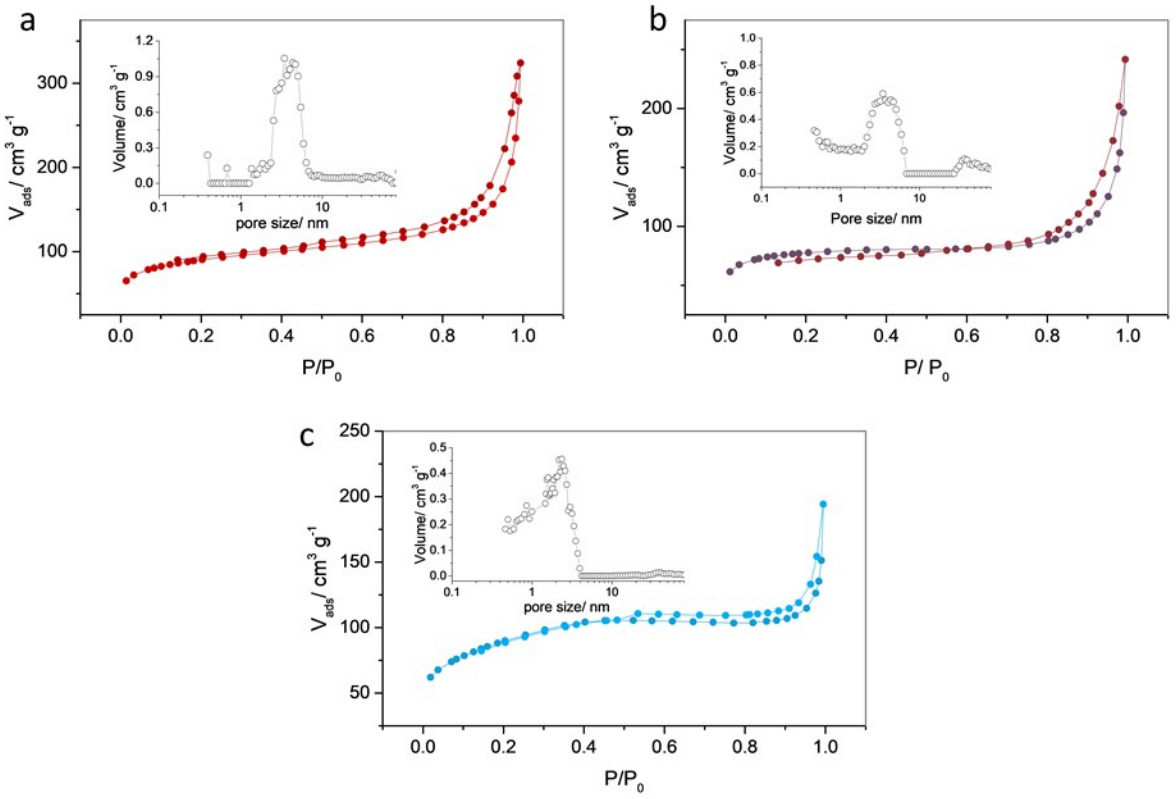

Fig. S5 BET analyses of C, TiO_2-TiN/C and C/TiO_2-TiN hollow spheres. Isothermal curves and pore size distributions of (a) C, (b) TiO_2-TiN/C and (c) C/TiO_2-TiN hollow spheres. The specific surface areas and average pore sizes are for hollow C, TiO_2-TiN/C and C/TiO_2-TiN are 313.3 m^2 g^{-1}/4 nm, 268.1 m^2 g^{-1}/3.5 nm and 244.9 m^2 g^{-1}/2.6 nm, respectively. The large surface area and mesopores are beneficial for the infusion of sulfur particles inside. Note that the average pore sizes are larger than the dimensions of polysulfides, thus it is expected that the marginally different pore sizes of these three host would not significantly affect the polysulfide diffusion behaviors.

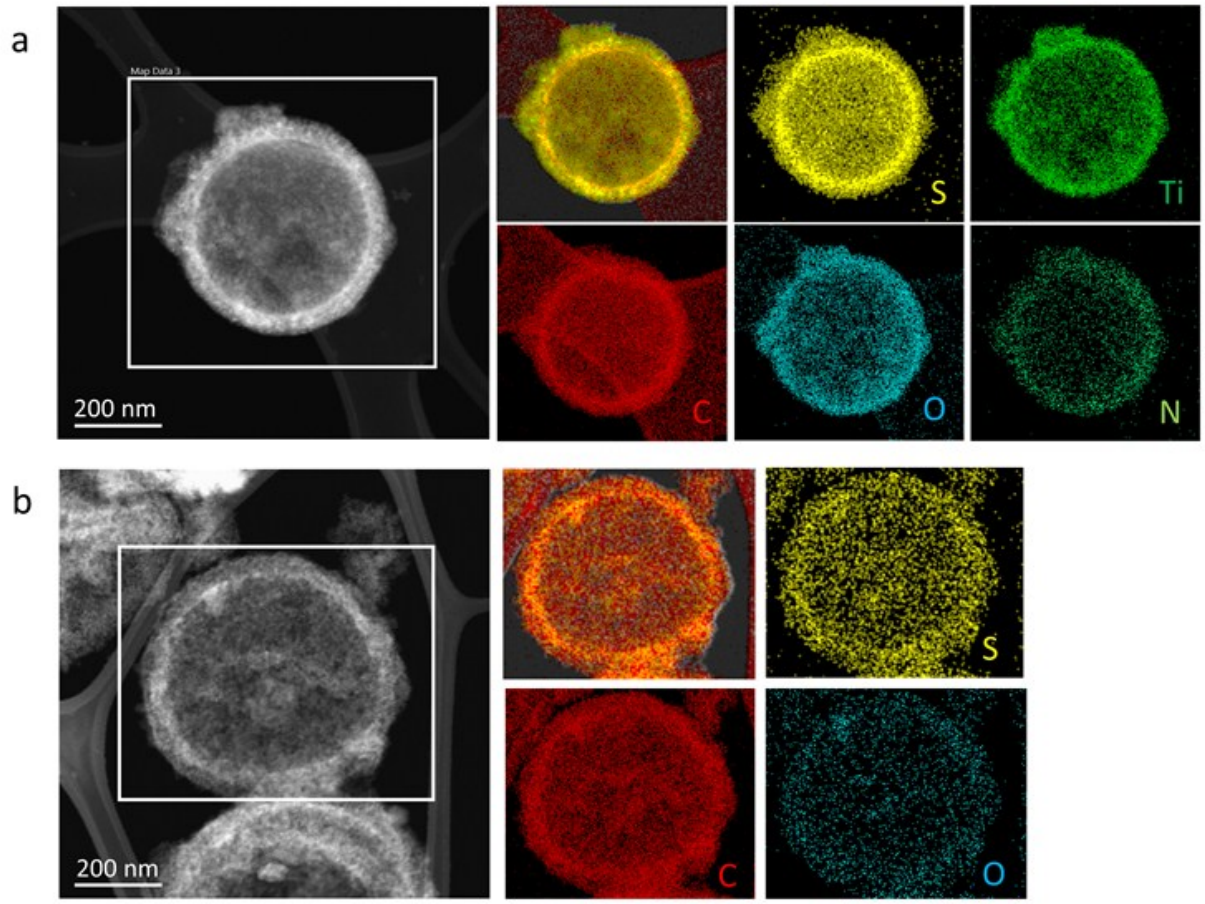

Fig. S6 STEM image and elemental mapping of TiO_2-TiN/C/S and C/S composites. (a) TiO_2-TiN/C/S and (b) C/S particles. It is noted that the hollow C is not fully filled with sulfur particles, which is intendedly designed to observe the diffusion of polysulfide and the formation of lithium sulfides at inner walls in liquid TEM study.

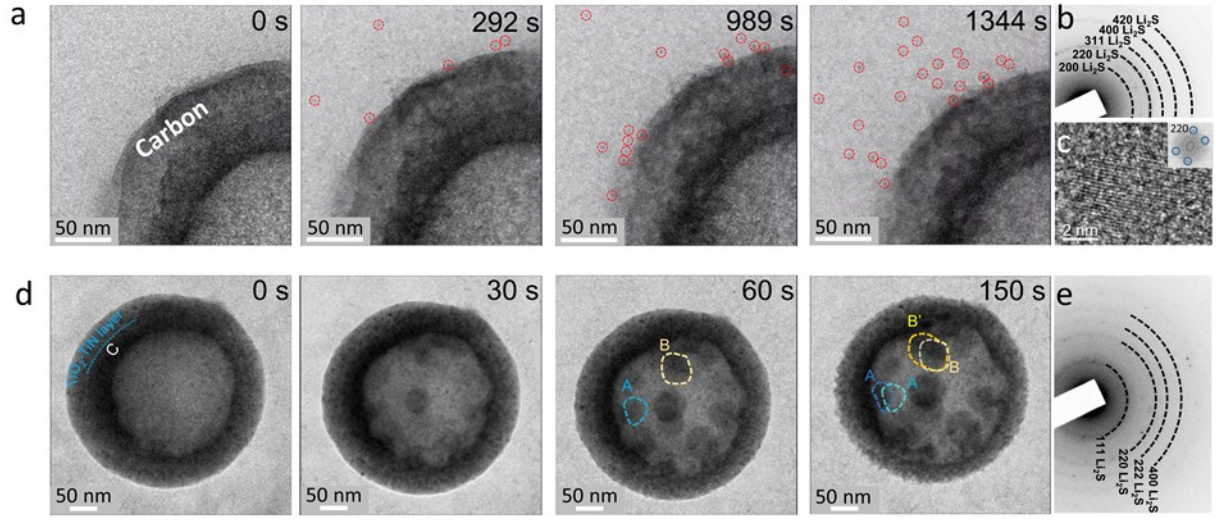

Fig. S7 *In-situ* TEM study of C/S and TiO_2-TiN/C/S particles. (a) Time-sequential TEM images of the lithiation of a C/S particle, the inset red circles refer to lithium sulfide particles diffusing out of C host, (b) SAED pattern of lithiated C/S, (c) HRTEM image of the lithium sulfide crystal out of C host; (d) time-sequential TEM images of the lithiation of a TiO_2-TiN/C/S particle, at 60 and 150 s, the de-attachment of particle #A and #B is observed, (e) SAED pattern of lithiated TiO_2-TiN/C/S, indicating the formation of Li_2S.

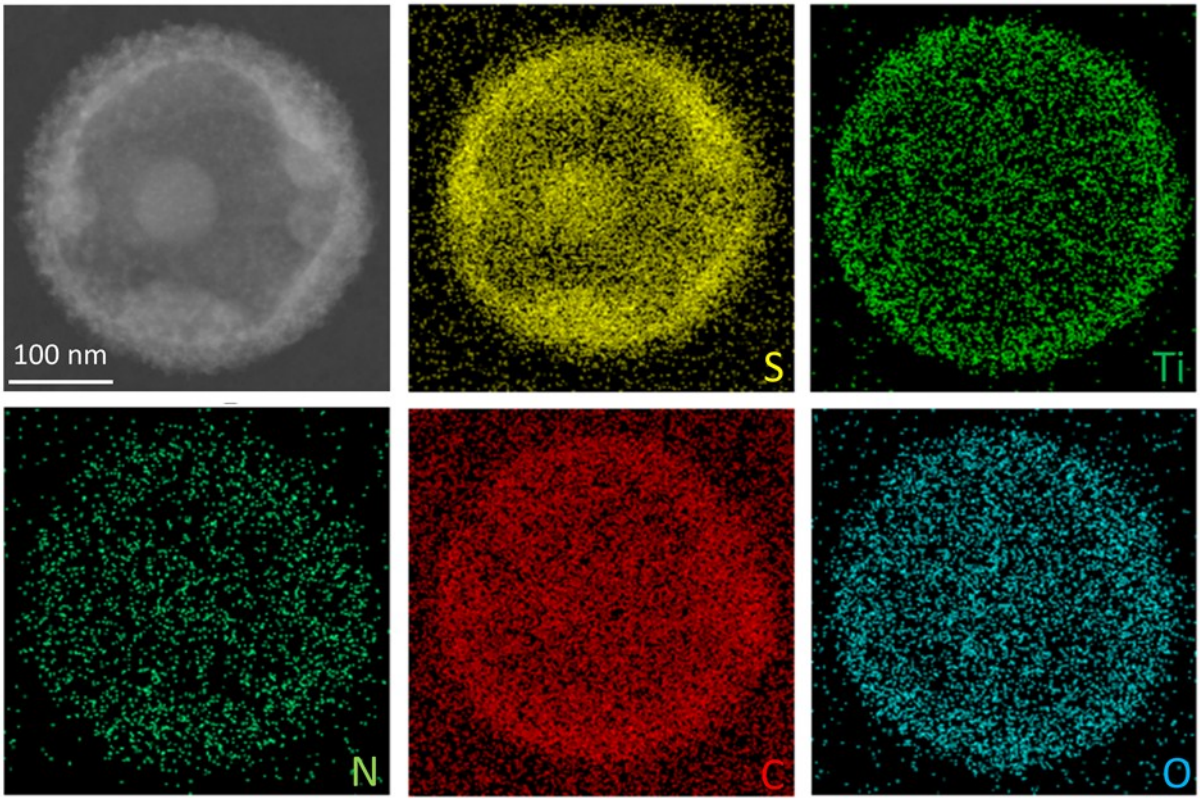

Fig. S8 STEM image and EDS mapping of a lithiated TiO_2-TiN/C/S particle in liquid TEM study. The signal from sulfur outside the particle is much negligible compared to that inside the particle, indicating that sulfur is well secured within the structure.

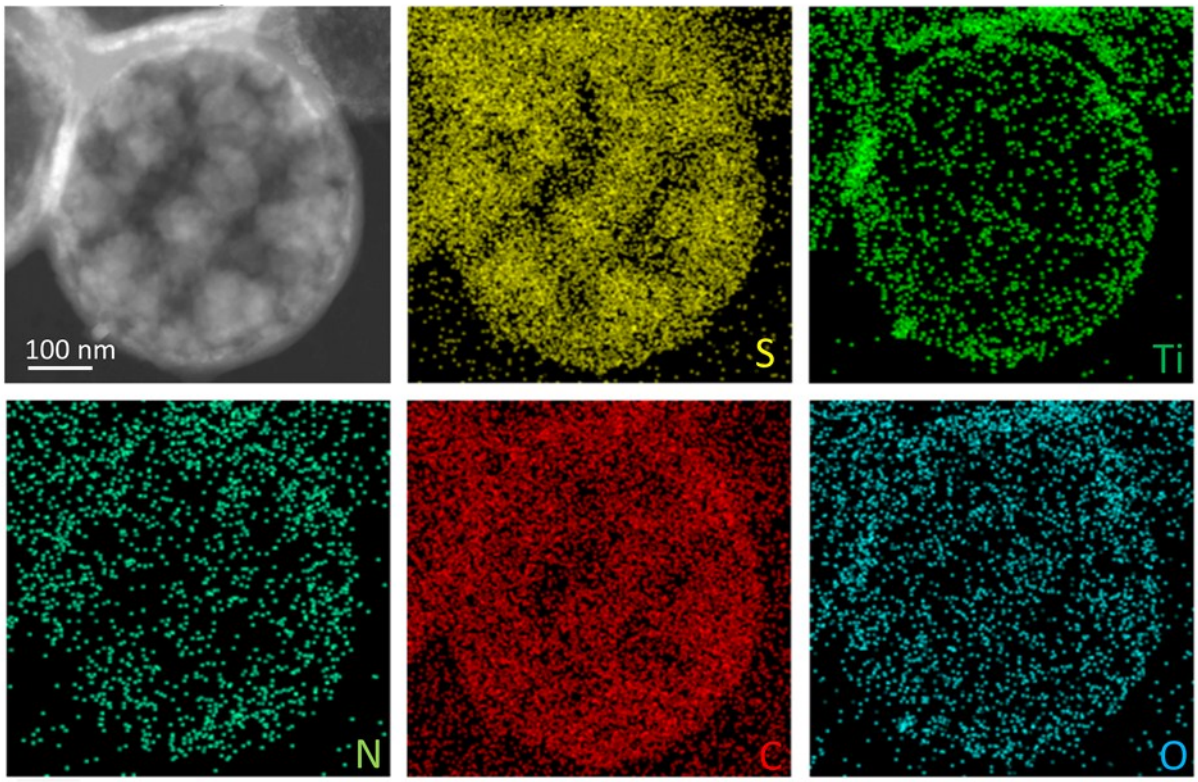

Fig. S9 STEM image and EDS mapping of a lithiated C/TiO_2-TiN/S particle in liquid TEM study.

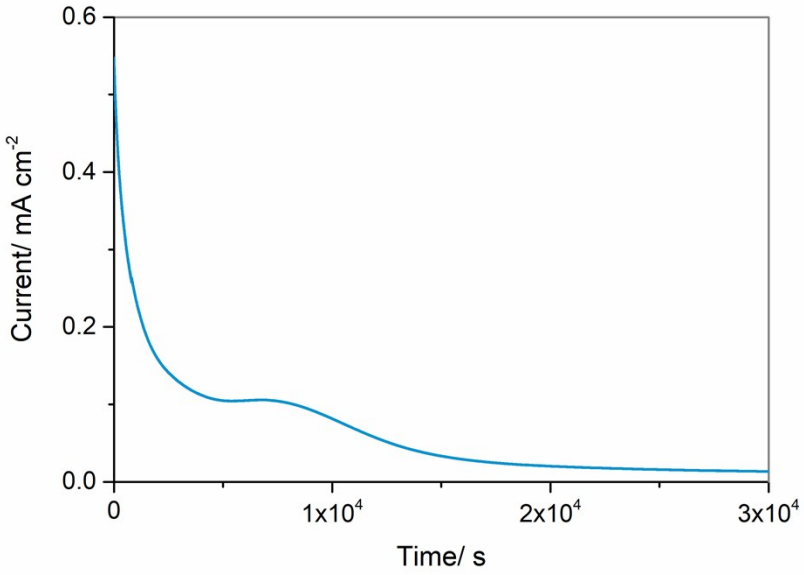

Fig. S10 Current *vs*. time curve for potentiostatic discharge of polysulfides at 2.05 V on TiO_2-TiN particles. The nucleation and growth of lithium sulfides on TiO_2-TiN particles was studied by potentiostatically discharge Li_2S_6 at a constant driving force of 10 mV, similar to our previous work.[1]

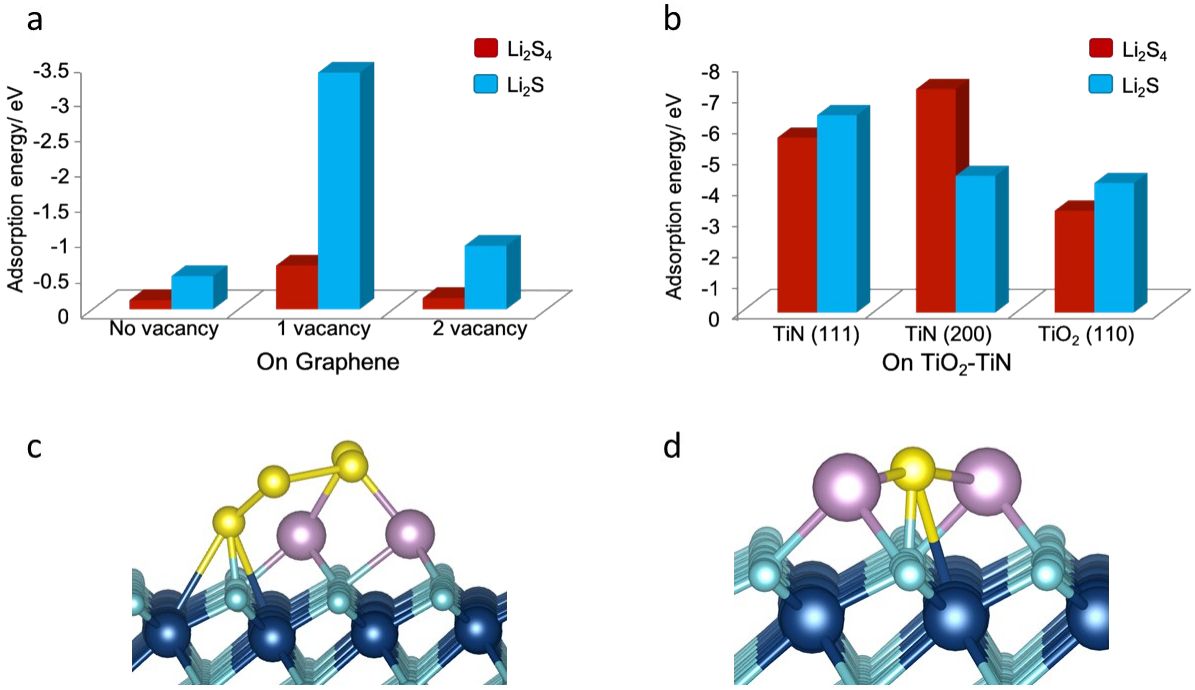

Fig. S11 DFT calculation of adsorption energies and configurations. Li_2S and Li_2S_4 adsorption energies on (a) graphene and (b) TiO_2 and TiN surfaces; optimized structures with the most stable configuration of (c) Li_2S_4 and (d) Li_2S adsorbed on a (111) TiN surface.

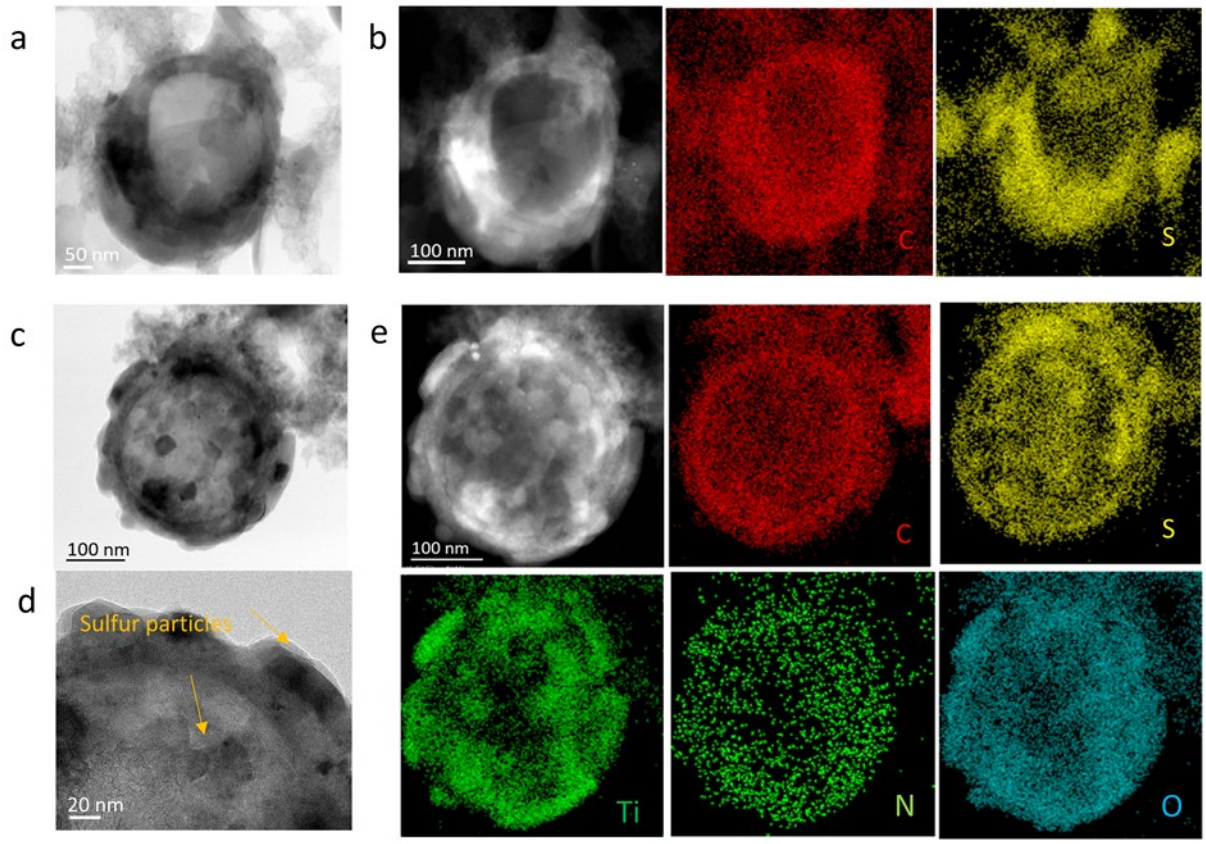

Fig. S12 TEM analysis of cycled C/S and TiO_2-TiN/C/S electrodes in Fig. 5b. (a) TEM image and (b) STEM image, EDS mapping of cycled C/S particles showing accumulation of sulfur particles outside of C hosts, consistent with the poor cyclic stability; (c-e) TEM images and EDS mapping of cycled TiO_2-TiN/C/S particles showing that most of the sulfur particles are encapsulated within TiO_2-TiN/C, but some sulfur particles are attached on the outside TiO_2-TiN wall. The outer sulfur would be attributed to polysulfide adsorption by TiO_2-TiN outer wall during cycles.

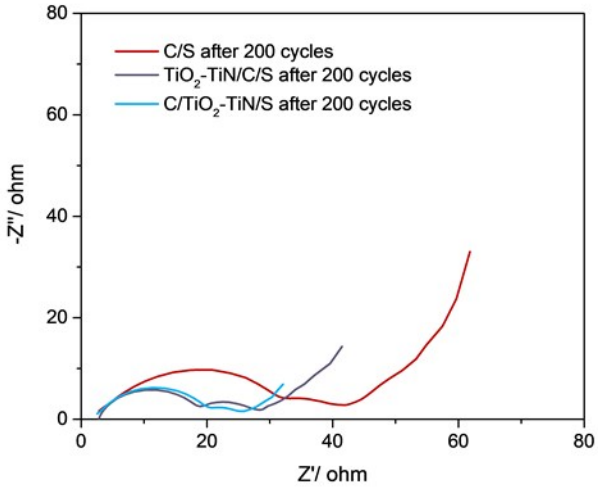

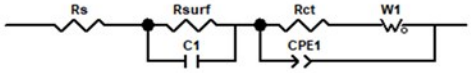

	R_0/ ohm	R_{surf} /ohm	R_{ct} /ohm
C/S	1.4	31.5	14.7
TiO_2-TiN/C/S	1.3	17.2	10.1
C/TiO_2-TiN/S	1.4	15.6	6.2

Fig. S13 Nyquist plots of cycled C/S, TiO_2-TiN/C/S and C/TiO_2-TiN/S electrodes in Figure 5b. The Nyquist plots are fitted with an equivalent circuit model, where R_0, $R_{surf,}$ R_{ct} refers to series resistance, interfacial resistance and charge transfer resistance, respectively. [1] The fitting results are listed in the right table, where C/TiO_2-TiN/S after 200 cycles presents the lowest R_{ct}.

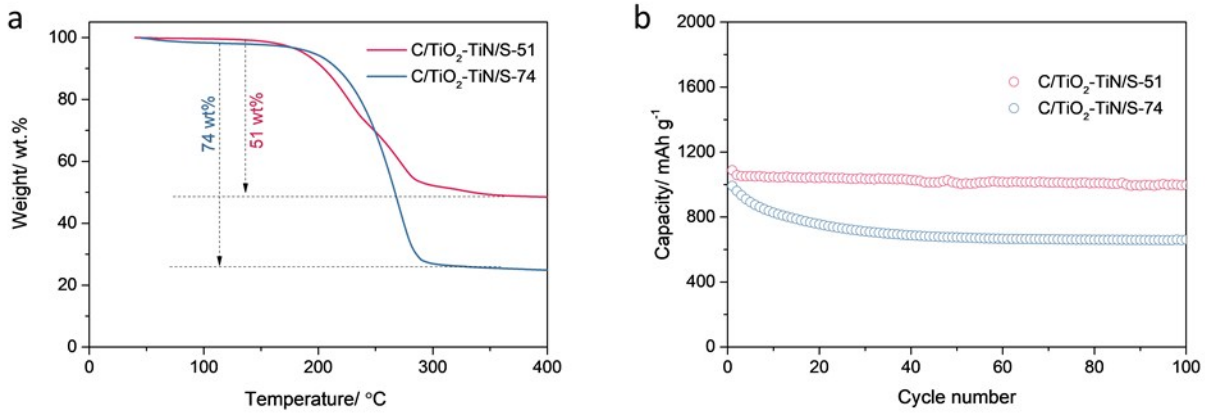

Fig. S14 Electrochemical performance of C/TiO_2-TiN/S with different sulfur content. (a) TGA curves of two C/TiO_2-TiN/S composites, which are designated as C/TiO_2-TiN/S-51 and C/TiO_2-TiN/S-74 based on their sulfur contents, (b) cyclic capacities of C/TiO_2-TiN/S-51 and C/TiO_2-TiN/S-74 at 0.2 C for 100 cycles. The capacity retentions of C/TiO_2-TiN/S-51 and C/TiO_2-TiN/S-74 are 92 % and 70 %, respectively. It signifies that C/TiO_2-TiN/S in the main context is close to the sweet spot for C/TiO_2-TiN host. The inferior cyclic stability of C/TiO_2-TiN/S-74 is possibly caused by volume expansion of sulfur particles or/and overflowing of polysulfides.

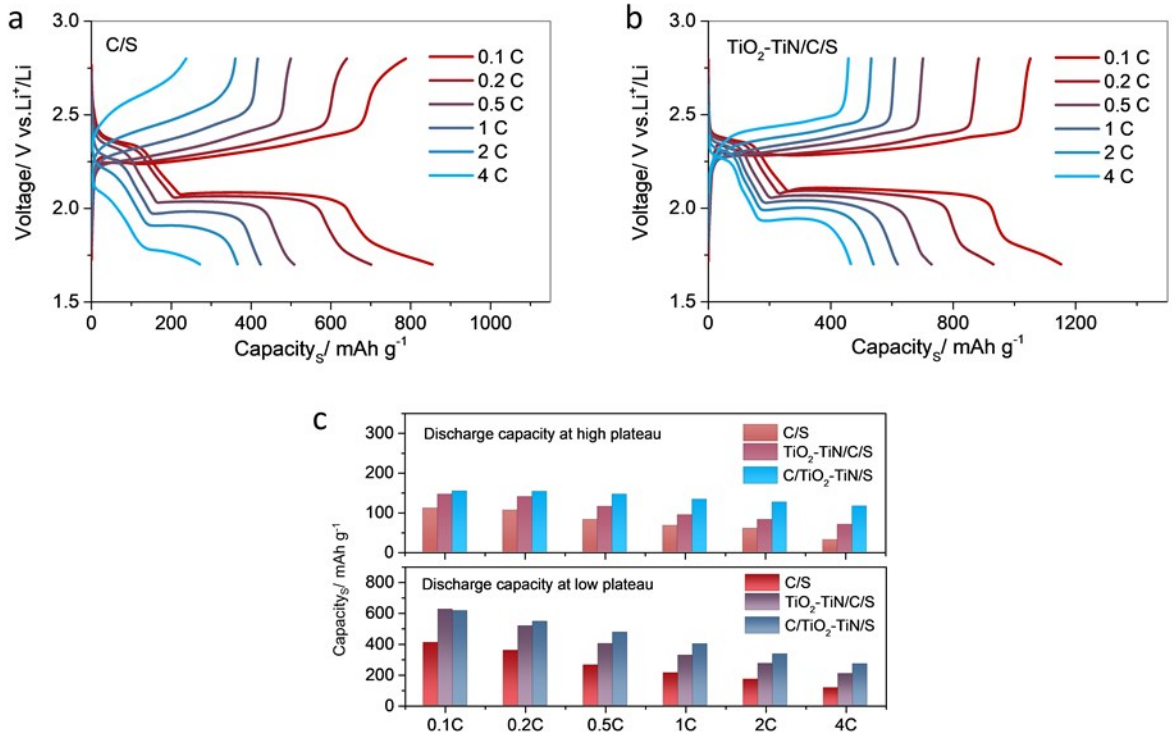

Fig. S15 Electrochemical characterizations of the C/S, TiO_2-TiN/C/S and C/TiO_2-TiN/S electrodes. Discharge/charge voltage profiles of (a) C/S and (b) TiO_2-TiN/C/S electrodes at different C rates, (c) high plateau (about 2.4V referring to formation of long chain polysulfides) and low plateau (about 2.1 V corresponding to reduction of polysulfides to lithium sulfides) discharge capacities derived from the rate performance.[1] The high plateau discharge capacity at 4 C for C/TiO_2-TiN/S maintains 77% of the capacity at 0.1 C, which is far higher than 50% for TiO_2-TiN/C/S and 27% for C/S electrodes in (c), indicating the strong immobilization of polysulfides induced by a C/TiO_2-TiN host. It is observed that the low plateau discharge capacity decreases by ~45% from 614 mAh g^{-1} at 0.1 C to 277 mAh g^{-1} at 4 C, which is lower than the 67% for TiO_2-TiN/C/S and 72% for C/S electrodes. The high capacity retention at a low discharge plateau suggests the facilitated nucleation and growth of lithium sulfides catalyzed by the TiO_2-TiN inner wall.

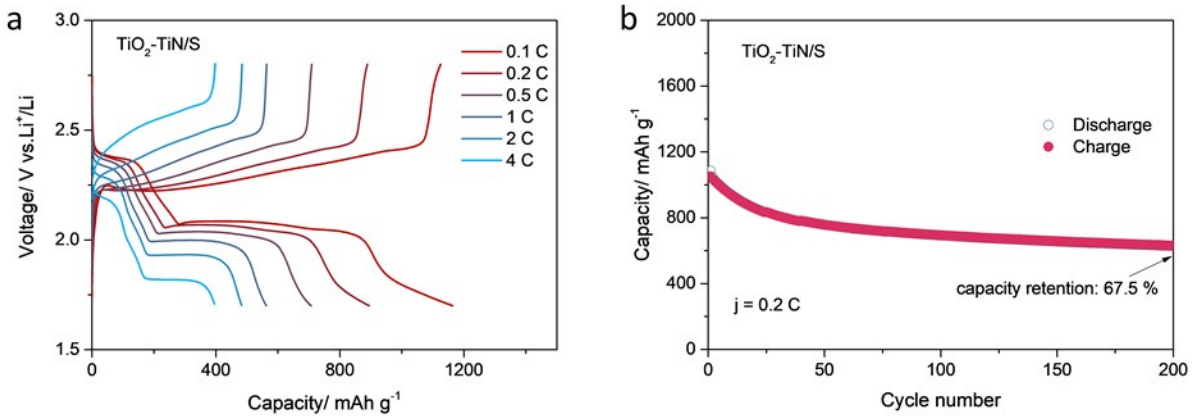

Fig. S16 Electrochemical characterizations of TiO_2-TiN/S electrodes. (a) Discharge/charge voltage profiles at different C rates, (b) discharge/charge capacities at 0.2 C for 200 cycles of TiO_2-TiN/S electrodes. It is observed that TiO_2-TiN/S presents comparatively larger polarizations, lower rate and cyclic capacities than these for C/TiO_2-TiN/S, implying the importance of the conductive carbon coating.

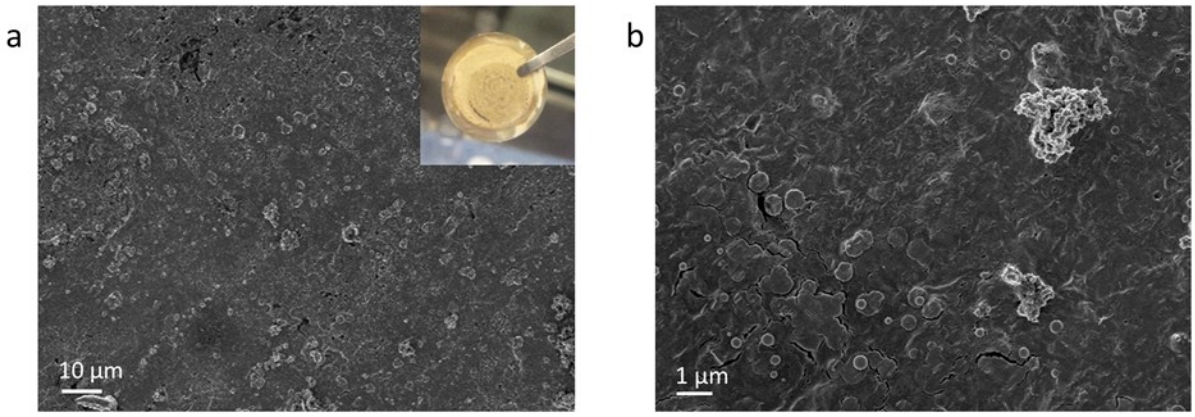

Fig. S17 Morphologies of Li metal of cycled cells in Fig. 5h. Optical and low magnification SEM images in (a) shows that neither the depletion of electrolyte nor the formation of large Li dendrites happens in the cycled LSBs at a high sulfur loading of 8 mg cm^{-2} and a low E/S ratio of 6.8 ml g^{-1}. Some small Li seeds are observed in high magnification SEM image (b), which are expected to be suppressed by high concentration electrolytes in future studies.

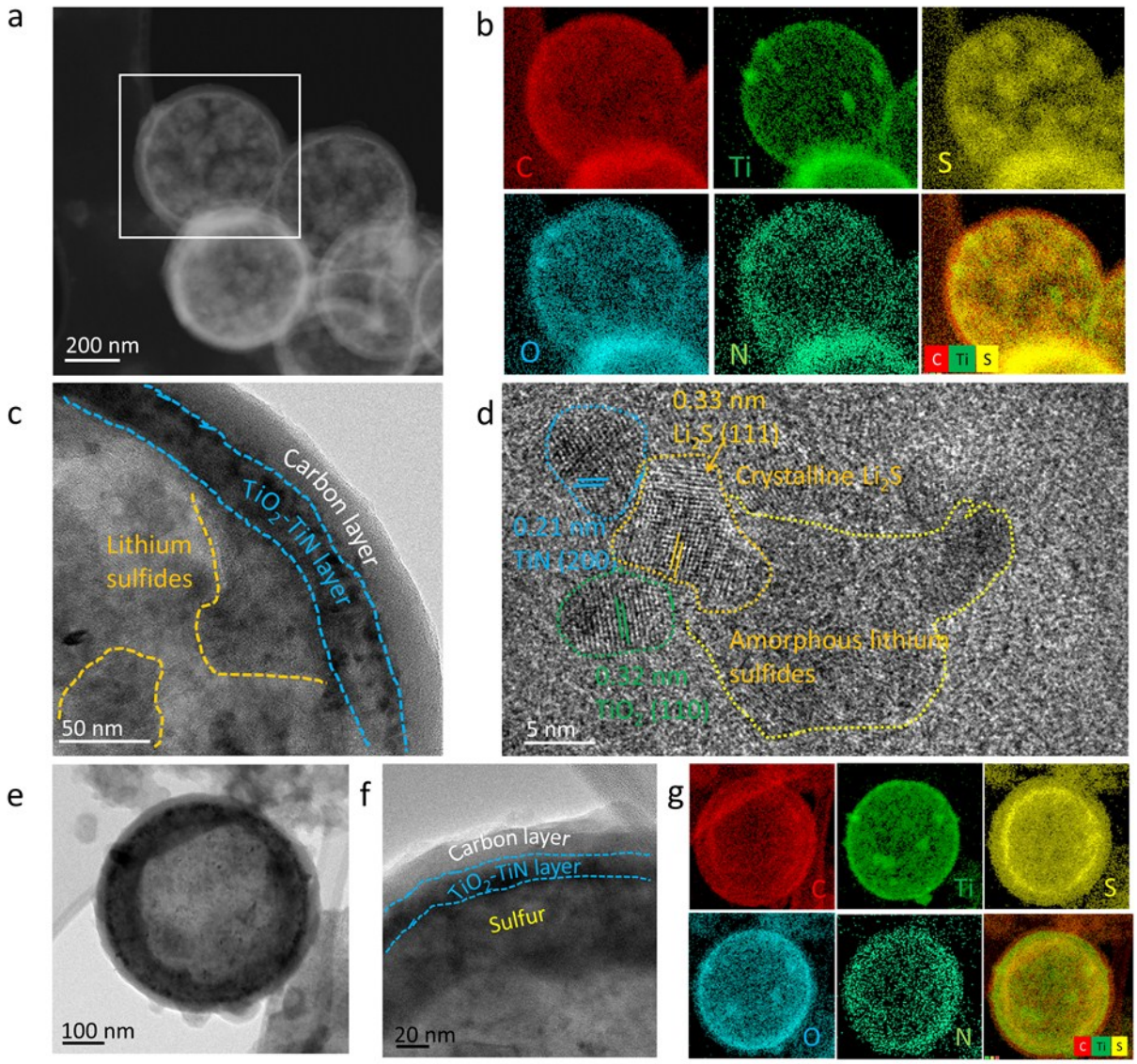

Fig. S18 *Ex-situ* TEM study of discharged and charged C/TiO_2-TiN/S electrodes. (a) STEM image and (b) EDS mapping of discharged C/TiO_2-TiN/S particles, (c), (d) HRTEM images of discharged C/TiO_2-TiN/S showing large lithium sulfides particles tightly attached to the polar TiO_2-TiN inner wall. The HRTEM image shows crystalline and amorphous lithium sulfides formed nearby the TiO_2-TiN crystals. All the information about lithium sulfides in the galvanostatically discharged C/TiO_2-TiN/S in real cells is in good agreement with the corresponding liquid *in-situ* TEM results. (e-g) TEM images and EDS mapping of charged C/TiO_2-TiN/S particle showing uniform sulfur film deposited on the inner wall of C/TiO_2-TiN/S particle, indicating excellent polysulfide immobilization during cycles.

Table S1 Comparison of the electrochemical performance of Li-S batteries with similar electrode materials.

Materials	E/S ratio µl mg^{-1}	Sulfur loading mg cm^{-2}	Electrochemical performance at high sulfur loading, capacity fading rate	Reference
TiN-TiO_2/G/LPS	10.3	4.3	1.42 mAh cm^{-2} after 2000 cycles, 0.017% per cycle	EES 2016[2]
Mesoporous TiN	/	1.0	0.6 mAh cm^{-2} after 500 cycles, 0.07 % per cycle	AM 2016[3]
TiO_2 NM/G/LPS	~20	3.2	~3.5 mAh cm^{-2} after 200 cycles, 0.04% per cycle	Nano Energy 2015[4]
Ti_4O_7/S	28-32	1.5-1.8	~1.8 mAh cm^{-2} after 100 cycles, 0.12 % per cycle	Nat. Commun. 2014[5]
TiO/C/S	25	4	~2.5 mAh cm^{-2} after 50 cycles, /	Nat. Commun. 2016[6]
TiO/carbon fiber/S	~25	5	~3.5 mAh cm^{-2} after 400 cycles, 0.085 % per cycle	Joule 2017[7]
VN/graphene/LPS	~30	3	~2.7 mAh cm^{-2} after 200 cycles, 0.1 % per cycle	Nat. Commun. 2017[8]
G/hollow carbon/S	~15	5	~5.7 mAh cm^{-2} after 50 cycles, ~0.58 % per cycle	Nat. Commun. 2017[9]
MOF/CNT/S	/	4.57	~3.5 mAh cm^{-2} after 200 cycles, /	Nat. Commun. 2017[10]
Authraquinone/G/S	~12	~1.8	~1.2 mAh cm^{-2} after 300 cycles, ~0.09 % per cycle	Nat. Commun. 2018[11]
CMK-3/S	~5	2	~1.4 mAh cm^{-2} after 100 cycles, 0.45 % per cycle	Nat. Energy 2018[12]
VO_2-VN/G/S	~7.5	4.2	~4.1 mAh cm^{-2} after 50 cycles, 0.85 % per cycle	EES 2018[13]
C/TiO_2-TiN/S	~6.8	8	~4.3 mAh cm^{-2} after 400 cycles, 0.05 % per cycle	This work

Supplementary Movies

Movie S1 | Liquid *in-situ* TEM observation of the lithiation of C/S particles.

Movie S2 | Liquid *in-situ* TEM observation of the lithiation of TiO_2-TiN/C/S particles.

Movie S3 | Liquid *in-situ* TEM observation of the lithiation of C/TiO_2-TiN/S particles.

Supplementary Methods

The first principle calculations were performed using DFT implemented in the Vienna *ab* initio simulation package (VASP)[14] with the generalized gradient approximation as parameterized by Perdew, Burke, and Ernzerhof (GGA-PBE).[15] The projector augmented wave (PAW) method[16] was used to describe the interactions between valence and core electrons. An effective Hubbard U value of 4.2 eV was used for d orbitals of Ti, which was determined by previous studies.[2] All surfaces were constructed based on the optimized bulk unit cell and ionic positions of each structure were fully relaxed with a fixed unit cell. The interface structures were modeled by a super-cell containing *n* layers of (110) Li_2S plane on 7 layers of (200) TiN plane and 5 layers of (110) TiO_2 plane with vacuum space larger than 10 Å respectively. Li_2S_4 and Li_2S molecule structures were optimized using a Gaussian 09 package from the previous study.[17]

All bulk, surface, and interface were calculated under the same exact condition: the cutoff energy was set to 400 eV, and spin-polarized DFT calculation was performed. For all systems, a Γ-point centered with k-point density of ~0.03 length of reciprocal lattice was used. A vacuum slab of about 10 Å was inserted between the surface slabs and interface slabs to remove any possible interaction between the slabs. The adsorption energy was defined as $E_{ads} = E_{total} - E_{Li_2S_x} - E_{surface}$, where E_{total} is the total energy of the adsorbed structure, $E_{Li_2S_x}$is the energy of Li_2S, and Li_2S_4 molecules under vacuum, and $E_{surface}$ is the energy of optimized graphene, TiN, and TiO_2 surfaces. The interfacial formation energy (γ) was calculated as: $\gamma = \frac{E_{Li_2S/PS} - E_{Li_2S} - E_{PS}}{A} - \sigma_{PS} - \sigma_{Li_2S}$, where $E_{Li_2S/PS}$ is the total energy of the Li_2S/TiO_2 or Li_2S/TiN supercell slab embedded in vacuum, and E_{Li_2S} and E_{PS} are the total energies of the

Li_2S and polar surface (*i.e.* TiO_2 or TiN) slabs with free surface respectively. *A* is the area of the interface, and σ_x is the surface energy defined as: $\sigma_x = \frac{E_x - E_x^{Bulk}}{2A}$, where E_x^{Bulk} stands for the total energy of Li_2S, TiO_2 or TiN in a bulk state.

Supplementary references

1. Xu, Z. L. *et al.* Exceptional catalytic effects of black phosphorus quantum dots in shuttling-free lithium sulfur batteries. *Nat. Commun.* **9,** 4164 (2018).

2. Zhou, T. *et al.* Twinborn TiO_2–TiN heterostructures enabling smooth trapping–diffusion–conversion of polysulfides towards ultralong life lithium–sulfur batteries. *Energy Environ. Sci.* **10,** 1694–1703 (2017).

3. Cui, Z., Zu, C., Zhou, W., Manthiram, A. & Goodenough, J. B. Mesoporous titanium nitride-enabled highly stable lithium-sulfur batteries. *Adv. Mater.* **28,** 6926–6931 (2016).

4. Zhou, G., Zhao, Y., Zu, C., Manthiram, A. Free-standing TiO_2 nanowire-embeded graphene hybrid membrane for advanced Li/dissolved polysulfide batteries. *Nano Energy* 1**2,** 240–249 (2015).

5. Pang, Q., Kundu, D., Cuisinier, M. & Nazar, L. F. Surface-enhanced redox chemistry of polysulphides on a metallic and polar host for lithium-sulphur batteries. *Nat. Commun.* **5,** 4759 (2014).

6. Li, Z. *et al.* A sulfur host based on titanium monoxide@carbon hollow spheres for advanced lithium–sulfur batteries. *Nat. Commun.* **7,** 13065 (2016).

7. Li, Z., Guan, B. Y., Zhang, J. & Lou, X. W. (David). A compact nanoconfined sulfur cathode for high-performance lithium-sulfur batteries. *Joule* **1,** 576–587 (2017).

8. Sun, Z. *et al.* Conductive porous vanadium nitride/graphene composite as chemical anchor of polysulfides for lithium-sulfur batteries. *Nat. Commun.* **8,** 14627 (2017).

9. Pei, F. *et al.* Self-supporting sulfur cathodes enabled by two-dimensional carbon yolk-shell

nanosheets for high-energy-density lithium-sulfur batteries. *Nat. Commun.* **8,** 482 (2017).

10. Mao, Y. *et al.* Foldable interpenetrated metal-organic frameworks/carbon nanotubes thin film for lithium–sulfur batteries. *Nat. Commun.* **8,** 14628 (2017).

11. Li, G. *et al.* Chemisorption of polysulfides through redox reactions with organic molecules for lithium–sulfur batteries. *Nat. Commun.* **9,** 705 (2018).

12. Pang, Q. *et al.* Tuning the electrolyte network structure to invoke quasi-solid state sulfur conversion and suppress lithium dendrite formation in Li–S batteries. *Nat. Energy* **3,** 783–791 (2018).

13. Song, Y. *et al.* Synchronous immobilization and conversion of polysulfides on a VO_2–VN binary host targeting high sulfur load Li–S batteries. *Energy Environ. Sci.* **11,** 2620–2630 (2018).

14. Kresse, G. & Furthmüller, J. Efficiency of ab-initio total energy calculations for metals and semiconductors using a plane-wave basis set. *Comput. Mater. Sci.* **6,** 15–50 (1996).

15. Perdew, J. P., Burke, K. & Ernzerhof, M. Generalized gradient approximation made simple. *Phys. Rev. Lett.* **77,** 3865–3868 (1996).

16. Blöchl, P. E. Projector augmented-wave method. *Phys. Rev. B* **50,** 17953–17979 (1994).

17. Tan, G. *et al.* Burning lithium in CS_2 for high-performing compact Li_2S–graphene nanocapsules for Li–S batteries. *Nat. Energy* **2,** 17090 (2017).